

<https://doi.org/10.1038/s41534-025-00972-8>

Tantalum airbridges for scalable superconducting quantum processors



Kunliang Bu^{1,2}, Sainan Huai^{1,2}, Zhenxing Zhang^{1,2}, Dengfeng Li¹, Yuan Li¹, Jingjing Hu¹, Xiaopei Yang¹, Maochun Dai¹✉, Tianqi Cai¹✉, Yi-Cong Zheng¹✉ & Shengyu Zhang¹

The unique property of tantalum, particularly its exceptional resistance to both acid and alkali, makes it promising for superconducting quantum processors. Here, we propose a novel lift-off method for fabricating tantalum airbridges with separate or fully-capped structures. This method introduces an aluminum film as a barrier layer to separate two layers of photoresist, which is then etched away before depositing tantalum film. We experimentally characterize these tantalum airbridges as control line jumpers, ground plane crossovers and coupling elements, and further validate the overall adaptability by a 13-qubit quantum processor with a median T_1 exceeding 100 μ s. The median single-qubit gate fidelity is measured at 99.95(2)% for isolated Randomized Benchmarking and 99.94(2)% for the simultaneous one. Additionally, the experimental achievement of airbridge coupling with a controlled-Z gate fidelity surpassing 99.2(2)% in a separate two-qubit quantum chip may facilitate scalable quantum computation and quantum error correction with entirely tantalum elements.

A high-performance superconducting quantum processor is crucial for achieving universal quantum computation. Various factors, including material platforms¹, introduced two-level systems (TLSs)^{2–4}, and low-temperature measurement environments^{5,6} impact the performance of a quantum chip. Recently, tantalum (Ta) has emerged as a promising material for superconducting qubit systems due to its superior stability in fabrication compared to commonly used materials such as aluminum (Al) and niobium (Nb)^{7–10}. Empirical evidence has indicated that these materials are all capable of achieving extended qubit coherence times^{6,11,12}. In particular, transmon qubits made with tantalum-based materials have been experimentally demonstrated to achieve average coherence time on the order of several hundred microseconds^{1,13,14}.

Airbridges, free-standing metallic crossovers with either separate or fully-capped structures, are widely used in superconducting quantum processors. They primarily serve as ground plane crossovers on either side of signal lines, improving coherence for both coplanar waveguide (CPW) resonators and qubits by equalizing the potential difference across CPW resonators and mitigating slot-line modes^{7,15–22}. Additionally, airbridges can function as control line jumpers or coupling elements, facilitating signal transmission and thereby increasing the wiring or coupling density through spatial architectures²³. These capabilities indicate promising future applications as airbridge technology continues to evolve. For instance, when utilized in coupling components, airbridges may enable non-local coupling among superconducting qubits, potentially reducing the circuit depth of

quantum algorithms and advancing various quantum error correction strategies.

Several fabrication techniques have been developed for constructing airbridges in previous work, including etching⁷, vapor HF release¹⁵, multi-layer photoresist lift-off¹⁸, and grayscale lithography^{20,21}. However, most existing techniques are applicable to aluminum. The development of reliable methods for fabricating tantalum airbridges, assessing the associated losses, and determining their impact on signal and qubit coherence in multiqubit chips are areas that require further exploration and validation.

In this work, we propose and demonstrate a novel lift-off method to fabricate airbridges with two layers of photoresist, compatible with all known superconducting materials and particularly suitable for tantalum. An aluminum film barrier layer is initially introduced as a sacrificial layer and partially removed prior to the film deposition process. The second layer of photoresist is subsequently applied while preserving the integrity of the airbridge scaffolds. Notably, tantalum film-based quantum chips with tantalum airbridges can be further cleaned using a piranha solution to eliminate residual photoresist and particles. We evaluate the performance and versatility of these tantalum airbridges as control line jumpers and ground plane crossovers through connectivity tests, measurements of the internal quality factor Q_i for CPW resonators, and characterization of microwave/flux crosstalk. The results show that the added capacitive loss per bridge is measured to be $(3.84 \pm 0.08) \times 10^{-9}$ at the single-photon level. For signal crosstalk, we find on-resonant microwave crosstalk better than -30 dB (median -45 dB) and flux crosstalk less than 9.7×10^{-4}

¹Tencent Quantum Laboratory, Tencent, Shenzhen, Guangdong, China. ²These authors contributed equally: Kunliang Bu, Sainan Huai, Zhenxing Zhang.

✉e-mail: maochundai@tencent.com; tianqicai@tencent.com; yicongzheng@tencent.com

(median 1.4×10^{-4}). To further illustrate the scalability and adaptability of tantalum airbridges in multiqubit fabrication processes, we present a tantalum film-based 13-qubit tunable coupling superconducting quantum processor equipped with fully-capped tantalum airbridges with a median T_1 exceeding 100 μ s. We carry out Randomized Benchmarking (RB) for all thirteen qubits, and the median single-qubit gate fidelity is measured to be approximately 99.95(2)% for isolated-RB and 99.94(2)% for simultaneous RB. Furthermore, considering the advantage of non-local coupling for fault-tolerant quantum computation^{24–29} and quantum simulation^{30–33}, we investigate direct qubit-qubit connections via tantalum airbridges by offering extra spatial coupling freedom. Our experiments demonstrate that tantalum airbridges effectively facilitate coupling between qubits without compromising coherence time, with two-qubit controlled-Z (CZ) gate fidelity achieving 99.2(2)% via RB³⁴. This study, therefore, provides a promising approach to the fabrication of high-performance quantum processors with tantalum-based elements.

Results

Fabrication procedure

The detailed fabrication procedure of tantalum airbridges is illustrated schematically in Fig. 1a–h. The CPW was first fabricated on a sapphire substrate with a 200 nm thick α -phase tantalum film^{1,13}. Due to exposure to the atmosphere, a native oxide layer naturally formed on the top surface. The base layer for airbridges was then developed after subjecting the first layer of photoresist (SPR220) to ultraviolet exposure, followed by a 140 °C reflow process to form an arch for mechanical stability, ensuring continuous connection between suspending crossovers and base layers⁷. Next, a 25 nm thick aluminum film was deposited as a barrier layer between the two layers of photoresist. Careful selection of the barrier layer thickness is necessary; a too-thin aluminum film could lead to cracks during high-speed spin coating, while a too-thick film could induce instability in small structures, especially for fully-capped airbridges during subsequent development processes. To define the bridge layer, a second layer of photoresist (either positive or negative type; SPR220 in our case) was applied on the barrier layer to construct the main structure of the airbridges. The barrier layer (sacrificial layer) was then etched away using TMAH (Tetramethylammonium hydroxide) alkali developer solution. Following this step, a 400 nm tantalum film was deposited onto the obtained structure using magnetron sputtering to form the bridge layer. Prior to deposition, we performed in situ argon ion milling for 2 min under a pressure of 1.0×10^{-4} Torr to remove any native oxide present on the base tantalum surface, ensuring proper electrical contact. After tantalum deposition, we applied ultrasonic treatment with deionized water to the samples, effectively destroying the fragile connection between airbridge base layers and nearby tantalum film on the sidewall of the photoresist. Specifically, another dip in a Transene Aluminum Etchant Type A solution could be selected to remove aluminum residue for tantalum airbridges. Finally, the sample was dipped in Remover PG to undergo the lift-off process, followed by plasma cleaning. The corresponding scanning electron microscope (SEM) images of the tantalum airbridges can be found in Fig. 1i, j (more details can be found in Supplementary Materials).

The presence of an aluminum barrier layer is necessary for the proposed lift-off method for several reasons. Firstly, it effectively prevents the mixing of the two layers of photoresist used in the recipe, as most types of photoresist are susceptible to blending, leading to pattern degradation during the spin coating of the second layer. Secondly, it provides protection for the arc-shaped scaffold created by the first layer of photoresist against exposure to the second one and eliminates potential damage caused by subsequent alkali development. Thirdly, after undergoing argon ion milling, a large amount of stubborn residual photoresist on sidewalls remains unremovable by solvents⁷. Fortunately, the barrier layer is usually over etched, leaving a small gap between the two layers of photoresist that effectively disconnects the stubborn residue and benefits a clean surface.

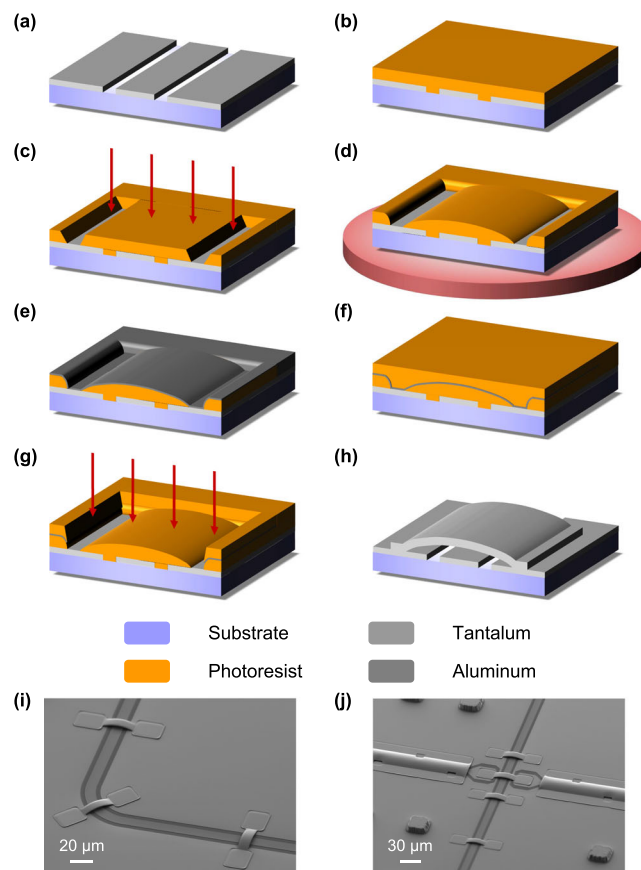


Fig. 1 | Schematic diagram of key processes in the fabrication of superconducting tantalum airbridges, with substrate shown in violet, tantalum in light gray, aluminum in dark gray, and photoresist in orange. a Fabrication of the CPW layer with a 200 nm thick α -phase tantalum film on the sapphire substrate. Formation of the photoresist scaffold and base layer for airbridges with **b** spin coating, **c** exposure and **d** reflow of the first layer of photoresist. The red arrows in **c** denote the ultraviolet light, while the red disk in **d** represents baking at 140 °C. **e** Deposition of a barrier layer with 25 nm thick aluminum film. Formation of the bridge layer with **f** spin coating and **g** exposure of the second layer of photoresist. **h** Deposition of the tantalum airbridge with the niobium functioned as the seed layer after the ion milling of the CPW to ensure an electrical connection. **i, j** SEM images of tantalum airbridges with separate and fully-capped structures connecting the ground planes or two CPW center lines by lift-off method.

In practice, etching⁷ and grayscale lithography^{20,21} methods can also be employed for the fabrication of tantalum airbridges in principle. However, they may impose more stringent conditions on the tantalum film deposition compared to the proposed lift-off method. Considering the poor temperature resistance of photoresist, tantalum can only be deposited at room or low temperature, assisted by utilizing niobium as a seed layer for airbridges^{35,36}. Meanwhile, corrugations may occur on the photoresist due to thermal effects during tantalum sputtering. Conversely, such thermal effects are absent in airbridge areas for the lift-off method since they contact the lower substrates, greatly simplifying the process.

Characteristics

To determine the appropriate design patterns and limits for fabricating airbridges, we systematically explored various lengths and widths using etching, grayscale lithography, and the proposed lift-off method. For airbridges with a height of 3 μ m, the maximum length for achieving structural stability is limited to 60 μ m based on etching and lift-off methods; however, when employing grayscale lithography, this limit can be extended to 200 μ m, as illustrated in Fig. 2a, b. This discrepancy arises from the observation that beyond the length of 60 μ m, plateaus appear in the profiles of

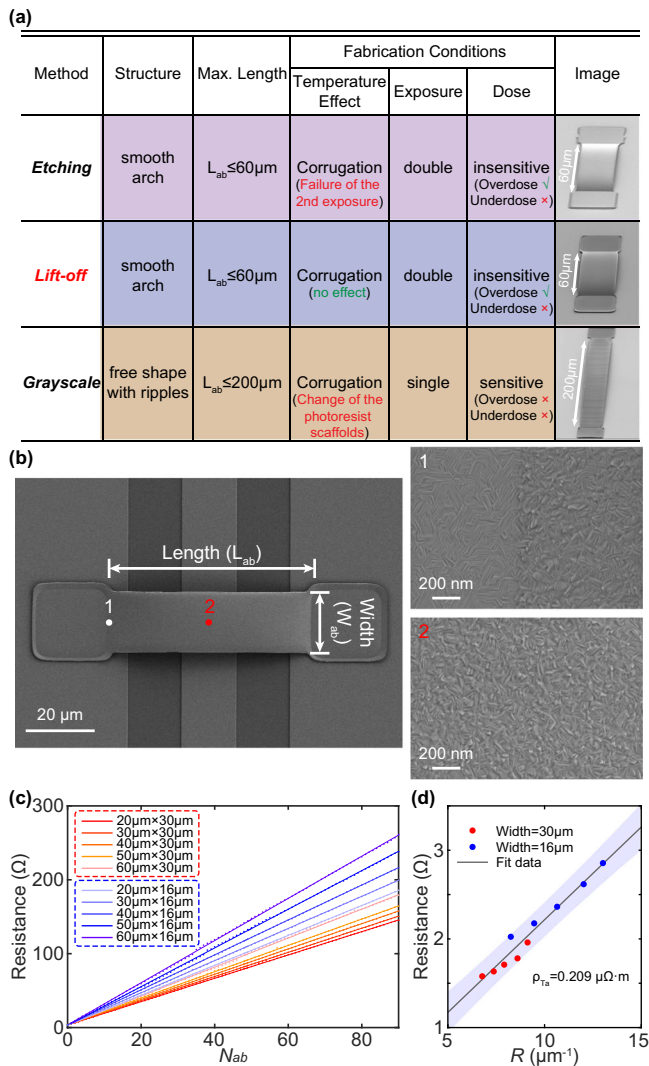


Fig. 2 | Characteristics of tantalum airbridges. **a** Comparison among three fabrication methods for airbridges, where the “Max. Length” in the table denotes the length limitation to ensure intact airbridges with a fixed height of 3 μm and arbitrary width, and the “Temperature Effect” in “Fabrication Conditions” represents the potential issues occurred due to heating during film deposition. **b** SEM images of a single tantalum airbridge with the full structure shown in left panel and zoom-in structures shown in right panel. The length (L_{ab}) and width (W_{ab}) of the airbridge are defined as the white arrow in the left panel. **c** Measured resistance versus number of airbridges (N_{ab}) with legend “ $L_{ab} \times W_{ab}$ ” of airbridges defined in **(b)**. **d** Resistance of single unit versus resistance ratio R . The red and blue dots represent raw data acquired from airbridges with width of 30 μm and 16 μm respectively. The fitted line includes the 95% confidence interval, which is indicated by the shaded area overlaid on the data.

photoresist scaffolds for those using etching or lift-off but not for grayscale lithography. We extracted the profile of photoresist sidewalls from a reflow surface and simulated scaffold profiles, which showed consistent evolution with experimental data (see Methods). This approach allows us to estimate the maximum length of an airbridge without conducting further experiments. In Fig. 2a, we compare these three methods, finding that the lift-off method is robust and fabrication-friendly, especially in constructing tantalum airbridges.

In addition, we carefully analyzed the crystal morphology of tantalum airbridges, as depicted in the right panel of Fig. 2b. The tantalum film on the base layer of airbridges shows a crystal grain similar to the α phase, while the tantalum film on top of airbridges differs from the typical α phase. The distinct grain structures observed at different positions can be attributed

to variations in growth bases for the tantalum film; specifically, α -phase tantalum (amorphous photoresist) serves as the base for tantalum film grown on the base (bridge) layer. Consequently, our results suggest that both the deposition environment and base materials significantly influence the phase of tantalum films.

Figure 2c demonstrates the measurement of resistance for tantalum airbridge chains to analyze the connectivity with varied lengths and widths. It is observed that the total resistance of tantalum airbridges scales linearly with the number of airbridges. Here, the slope of the fitted line represents the resistance of a single unit, comprising a tantalum airbridge and a conducting pad, and we define a total resistance ratio R for each single unit as

$$R = \frac{L_{ab}}{(W_{ab} \times t_{ab})} + \frac{L_{pad}}{(W_{pad} \times t_{pad})}, \quad (1)$$

where L_{ab} (L_{pad}), W_{ab} (W_{pad}), and t_{ab} (t_{pad}) denote the length, width, and thickness of the airbridge (conducting pad) respectively. The slope of the fitted line is then extracted and plotted against the total ratio, as depicted in Fig. 2d. This analysis yields a resistivity value of $\sim 0.21 \mu\Omega \cdot \text{m}$ for each single unit. The small resistivity indicates good contact using tantalum airbridges.

Q_i measurement

To quantify the added capacitive loss from the tantalum airbridges at low temperature ($\sim 20 \text{ mK}$ in the experiment), we fabricated a resonator chip containing seven $\lambda/4$ CPW resonators with various numbers of airbridges ranging from $N = 0$ to $N = 90$, as illustrated in Fig. 3a^{7,19}. The airbridges were designed with a length of 60 μm and width of 16 μm , automatically arranged at equal distances using our homemade electronic design automation (EDA) tool for each resonator³⁷. A zoom-in image displaying the arrangement of the airbridges is shown in Fig. 3b. Careful design considerations were taken into account for the resonators to ensure appropriate line width (also coupling quality factor Q_c) that facilitates subsequent measurement of the internal quality factor (Q_i). Furthermore, the resonance frequencies were uniformly distributed between 6.04 GHz and 6.64 GHz to avoid potential microwave electrical crosstalk¹⁹.

The internal quality factor Q_i was determined by measuring and fitting the S parameters of these resonators with varied drive power, allowing for a range of photon populations $\langle n_p \rangle$ in the resonator from single photon to high power photons³⁸. Figure 3c presents representative Q_i data for resonators with different numbers of airbridges. It is evident that at both low and high power, the trend of Q_i exhibits two plateaus corresponding to TLS-determined behavior at around the single-photon level and TLS-saturated behavior at high power level. Additionally, the quality factor of the resonator increases as the drive power increases, consistent with the loss in the resonator being dominated by the two-level states at the material interfaces³⁹, as depicted by the solid lines in Fig. 3c. For a tantalum resonator without added airbridges, the internal quality factor is measured to be 2.0×10^6 at single-photon power and increases to 5.3×10^7 at high photon power, consistent with the theoretical variation tendency. Similar trends are observed for tantalum resonators with a few tantalum airbridges. However, the overall Q_i values appear to decrease with an increasing number of airbridges, indicating additional loss introduced by tantalum airbridges that can be further characterized by fitting the loss tangent ($1/Q_i$) data. By observing the linear relationship between the number of airbridges and the loss tangent, we estimate an added loss per bridge of approximately $(3.84 \pm 0.08) \times 10^{-9}$, demonstrating comparable low-loss and high-quality performance of tantalum airbridges to aluminum airbridges^{7,19}.

Discussions

Our lift-off method for fabricating tantalum airbridges has been validated with a robust fabrication process, excellent connectivity, and minimal additional loss to the resonators. These findings suggest that they hold immense potential for widespread utilization in quantum processors^{40–42}. To further demonstrate their capabilities, we explore two areas: signal crosstalk using fully-capped tantalum airbridges and direct coupling element employing well-designed tantalum airbridges.

Fig. 3 | Q_i measurement of a resonator chip containing CPW resonators with various numbers of tantalum airbridges. **a** Optical micrograph of one resonator chip with varied tantalum airbridges. The number of airbridges increases from $N = 0$ to $N = 90$ and the resonance frequencies are uniformly distributed between 6.04 GHz and 6.64 GHz. All the airbridges were designed with a fixed length of $60\ \mu\text{m}$ and width of $16\ \mu\text{m}$, arranged at equal distances. **b** A zoom-in SEM image of the arranged tantalum airbridges circled by the red rectangle in (a). **c** Internal quality factor Q_i versus average photon population $\langle n_p \rangle$ for each resonator. The error bars represent the uncertainty of Q_i in the fitting process of S parameters. The solid lines are the fitting results obtained by the TLS model³⁹. Notice that the overall Q_i values tend to decline as the number of airbridges increases. **d** Loss tangent ($1/Q_i$) versus number of airbridges. The fitted slope of line represents the added capacitive loss caused by a single airbridge to the CPW resonator.

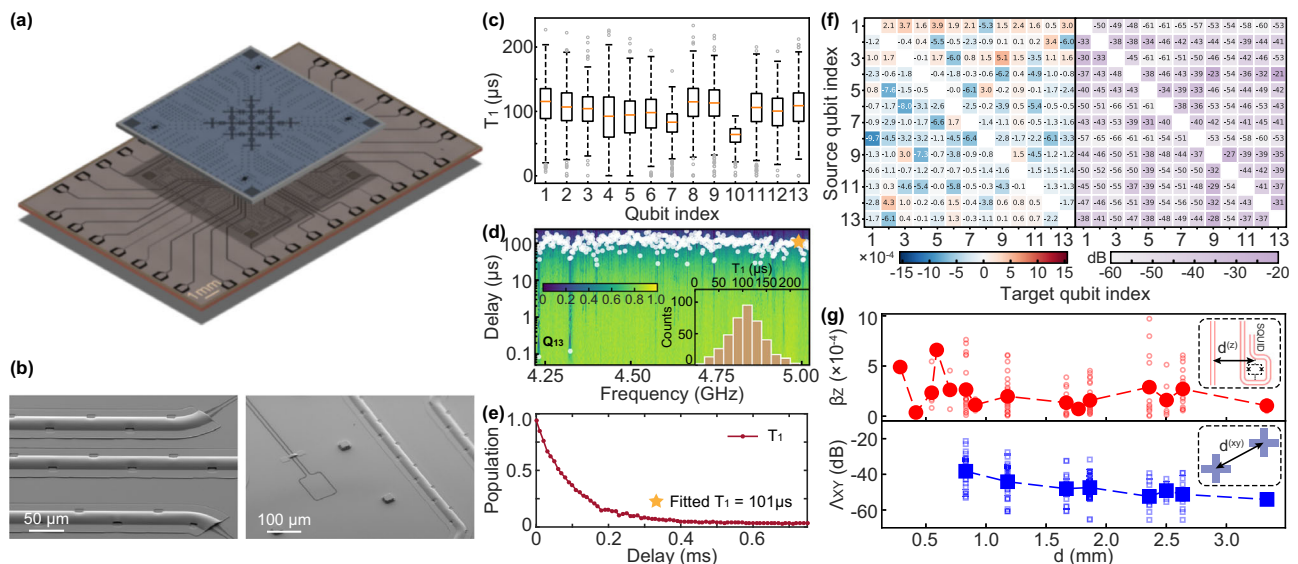
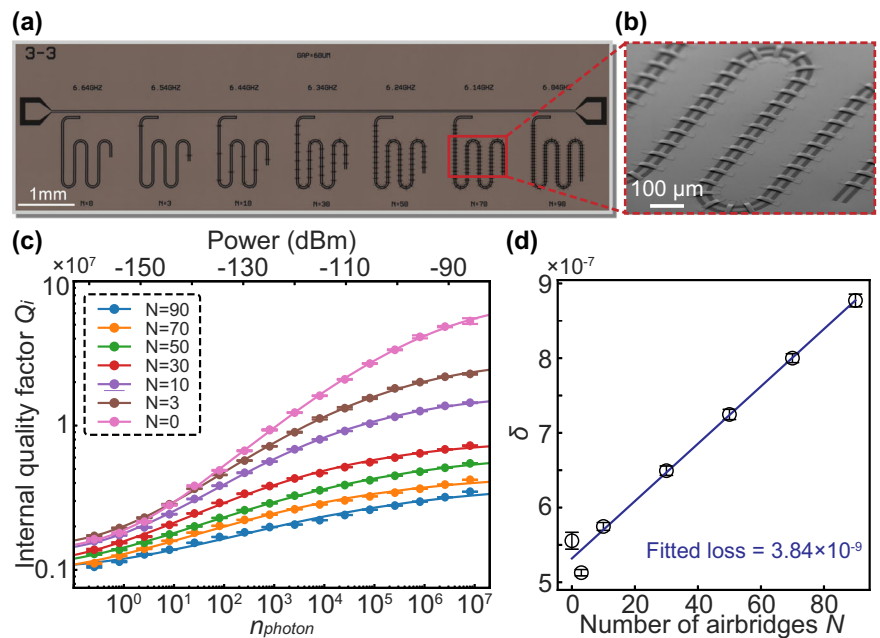


Fig. 4 | Investigation of tantalum airbridges in a tunable coupling superconducting quantum processor. **a** Optical micrograph of the 13-qubit flip-chip processor. Here, the top chip is primarily used for qubit layer containing both Josephson junctions and shunt capacitors, while the bottom chip comprises readout resonators and control lines. Tantalum airbridges with fully-capped structure are incorporated over each control line to minimize crosstalk. **b** SEM images of the tantalum airbridges with fully-capped structure in (a). **c** A box plot of T_1 results for all thirteen qubits, with a median T_1 exceeding $100\ \mu\text{s}$ for most qubits. Here, the box plot can illustrate the distribution of the data, with an interquartile range (IQR) of 1.5, indicating the range within which the middle 50% of the data lies. Meanwhile, the box represents the 25th percentile to the 75th

percentile, and the whiskers extend to the minimum and maximum values, excluding any outliers. **d** Characterization of T_1 measurement varied with qubit frequency for Q_{13} . The inset illustrates the histogram with a median T_1 of $109\ \mu\text{s}$. **e** A representative single T_1 measurement result marked in (d). **f** Measurement of flux crosstalk (left panel) and microwave crosstalk (right panel) with tantalum airbridges utilizing the fully-capped structure. **g** Distance dependence of the flux crosstalk β_z (top panel) and the microwave crosstalk Λ_{XY} (bottom panel). The inset provides definitions for the distance d relevant to both types of crosstalk. Specifically, $d^{(z)}$ represents the shortest distance from the target qubit (i.e., the target SQUID) to the flux line, while $d^{(xy)}$ is defined as the center separation between the target qubit and the source qubit.

We investigated the use of tantalum airbridges in a tunable coupling quantum processor based on a tantalum film and flip-chip architecture, which comprises 13 qubits and 16 couplers, as the schematic diagram shown in Fig. 4a^{43,44}. All computational qubits are frequency-tunable transmon qubits, with grounded couplers enabling continuous adjustment of the effective coupling strength between qubits^{45,46}. The design and optimization of the tantalum airbridges in this chip were achieved through a parametric EDA method, where the center line of the CPW can

be automatically identified for the chip layout with wiring, followed by adding the airbridges accordingly³⁷. The fabrication followed the proposed lift-off method depicted in Fig. 1 (the complete fabrication process of this 13-qubit quantum chip can be found in Supplementary Materials). Because of the resistance to acid and alkaline solutions, we could immerse the chip into piranha and HF solution to remove residual photoresist and eliminate the oxygen layer on the substrate after fabricating the tantalum airbridges—an option typically unavailable for aluminum airbridges.

SEM images showcasing fully-capped tantalum airbridges wrapped around control lines are presented in Fig. 4b.

The fundamental performance of this flip-chip processor was characterized, with the results illustrated in Fig. 4c. It can be observed that most qubits exhibit a median T_1 exceeding 100 μ s extracted from the T_1 distribution varied with qubit frequencies, see Fig. 4d as an example (Supplementary Materials provide complete data for other qubits). Meanwhile, a representative single T_1 measurement is depicted in Fig. 4e. Notably, when TLS occurs at certain frequencies, a significant decline in population may occur, bringing detrimental effect to qubits⁴⁷.

Moreover, we evaluated microwave and flux crosstalk between each control line. This crosstalk not only complicates the calibration of quantum circuits but also affects the fidelity of quantum gate operations, ultimately having a detrimental impact on the quantum computing process. Previous studies have indicated that crosstalk may be mitigated through active and passive methods, such as the implementation of a crosstalk matrix^{46,48–52}.

While this approach can effectively reduce crosstalk levels, it requires significant time and resources, particularly as the number of qubits increases due to the quadratic scaling of experiments⁴⁹. Here, we focus on the use of fully-capped airbridges, which provide complete coverage and shielding from microwave electrical signals^{7,40}. We conducted crosstalk measurements on the chip, and the corresponding results are presented in Fig. 4f, revealing flux crosstalk less than 9.7×10^{-4} (median 1.4×10^{-4}) and microwave crosstalk better than -30 dB (median -45 dB) (see Supplementary Materials for crosstalk measurement). To further explore the relationship between crosstalk and signal line separation, we sorted the crosstalk data in Fig. 4f combined with the distance between the target qubit and the source qubit. The results, shown in Fig. 4g, indicate that microwave crosstalk decreases with larger separation, with the fitted slope of average values being ~ -6.6 dB/mm for the 13-qubit quantum processor. However, flux crosstalk presents a fluctuation pattern, which seems to be uncorrelated with distance.

Additionally, we have also noted a recent study that thoroughly examined the factors influencing crosstalk in signal lines within a flip-chip architecture⁵³. By comparing quantum chips with and without airbridges, the authors analyzed the relationship between the suppression of microwave and flux crosstalk and the presence of fully-capped airbridges. Our findings align closely with theirs, particularly concerning the relationship between crosstalk and signal line separation. In fact, the mechanisms behind passive crosstalk suppression are complex. Current research does not definitively establish that fully-capped airbridges are always effective, as the factors influencing suppression are multifaceted. These factors may relate not only to the shielding effectiveness of the signal lines but also to the chip architecture (e.g., planar or flip-chip), the geometric structures on the chip (e.g., the routing of signal lines), the PCB of the sample box (including the inherent crosstalk of the PCB itself), and wire bonding techniques. Nevertheless, our experimental results offer valuable insights for future research on the impact of tantalum airbridges on crosstalk levels and their effectiveness in suppression.

We benchmark the single qubit gate fidelity using both isolated and simultaneous RB to assess the isolation of the fully-capped airbridges without compensating the microwave crosstalk. The median fidelity is found to be 99.95(2)% for isolated-RB and 99.94(2)% for simultaneous-RB. The similarity in these results suggests that our device exhibits low microwave crosstalk (see detailed data in Methods).

Furthermore, we discuss the coupling through airbridges. Superconducting qubits can typically be coupled through direct coupling⁵⁴, coupler coupling^{40,46}, resonator coupling³², or waveguide coupling^{55–57}. For instance, the well-known surface code requires nearest neighbor qubit coupling, rendering direct or coupler coupling suitable choices^{58,59}. However, long-distance qubit-qubit connections or fully-connected architecture requires the utilization of resonator or waveguide coupling. The resonators provide various geometrical options for connecting qubits but they also impose limitations on chip size and scalability. Recently, advancements in

error correction codes, particularly quantum low-density parity check codes, have necessitated non-local (non-neighboring) qubit couplings for syndrome measurements, achieving a reduction of overall resource requirements^{24–29}. Here, we propose a method for qubit interconnection using airbridges, which presents a potential solution for promoting non-local coupling by leveraging the spatial chip architectures.

Figure 5a illustrates a two-qubit superconducting quantum chip with tantalum airbridge-coupling fabricated via the lift-off method. We designed two groups of qubit pairs coupled with (experimental group) and without (control group) tantalum airbridges to benchmark the performance. We first characterized the effective coupling strength between these two qubits using airbridge coupling, as depicted in Fig. 5b. By tuning the frequency of one qubit to resonate with the other, the coupling strength can be extracted to be around 3.9 MHz, similar to that achieved in the control group. We then measured the coherence time of the qubits, as shown in Fig. 5c, finding that they are unlikely to be affected by introducing a tantalum airbridge for coupling, confirming its feasibility. Furthermore, the quality of such airbridge coupling was evaluated through a two-qubit CZ gate process. The flux pulses applied to each qubit were carefully designed with slowly changing waveforms and adjusted to generate resonance processes for states $|11\rangle$ and $|02\rangle$ (or $|20\rangle$), followed by the accumulation of a π phase, thereby realizing standard diabatic CZ gate operation^{60,61}. The fidelity for this two-qubit CZ gate was characterized through interleaved-RB, yielding 99.2(2)% as depicted in Fig. 5d, comparable to the one acquired from the control group. We also verified the entanglement capability by preparing a Bell state with such a CZ gate, achieving a state fidelity of 99.70% via quantum state tomography (QST), as illustrated in Fig. 5e.

Finally, we present schematic diagrams in Fig. 5f to illustrate the application of the proposed airbridge-coupling mechanism in a multi-qubit quantum chip featuring non-local couplings, where we propose two types of airbridges designed for effective coupling. It is crucial to consider potential spurious couplings when an airbridge spans over circuit elements within the quantum chip. For instance, when an airbridge crosses over a qubit, unintended capacitive interactions may occur, potentially causing the crossed qubit to act as a spectator qubit, which could adversely affect quantum gate operations between the qubits connected via the airbridge. To mitigate such effects, several strategies can be employed. One effective approach is to design the chip layout such that airbridges do not directly cross over qubits but rather over couplers. Since couplers typically remain unexcited during quantum operations and their idle frequencies are generally far removed from those of the qubits, the risk of spurious coupling induced by the airbridge can be significantly reduced. However, the issue of spurious coupling still warrants further investigation and research, particularly in the context of employing airbridges for non-local coupling processes⁶². Moreover, the long-distance airbridges depicted in Fig. 5f demonstrate the capability to span extensive distances on the chip, which could be critical for future applications in large-scale quantum computing and quantum error correction. Therefore, continued enhancements in airbridge design and fabrication techniques, including the development of new bridge structures⁶³ and the optimization of lift-off or grayscale lithography processes⁶², remain important areas for further exploration.

In summary, we propose and develop a novel lift-off method for fabricating tantalum airbridges with a separate and fully-capped structure. We compare three fabrication methods, including etching, grayscale lithography, and the proposed lift-off. We verify the robustness of our approach under varied fabrication conditions, with an emphasis on temperature control during film deposition. Furthermore, the excellent performance and versatility of these tantalum airbridges as control line jumpers and ground plane crossovers are illustrated through connectivity tests, Q_i measurement of CPW resonators, and crosstalk calibration. To demonstrate the scalability and adaptability of tantalum airbridges in multiqubit fabrication processes, we present a 13-qubit tunable coupling superconducting quantum processor

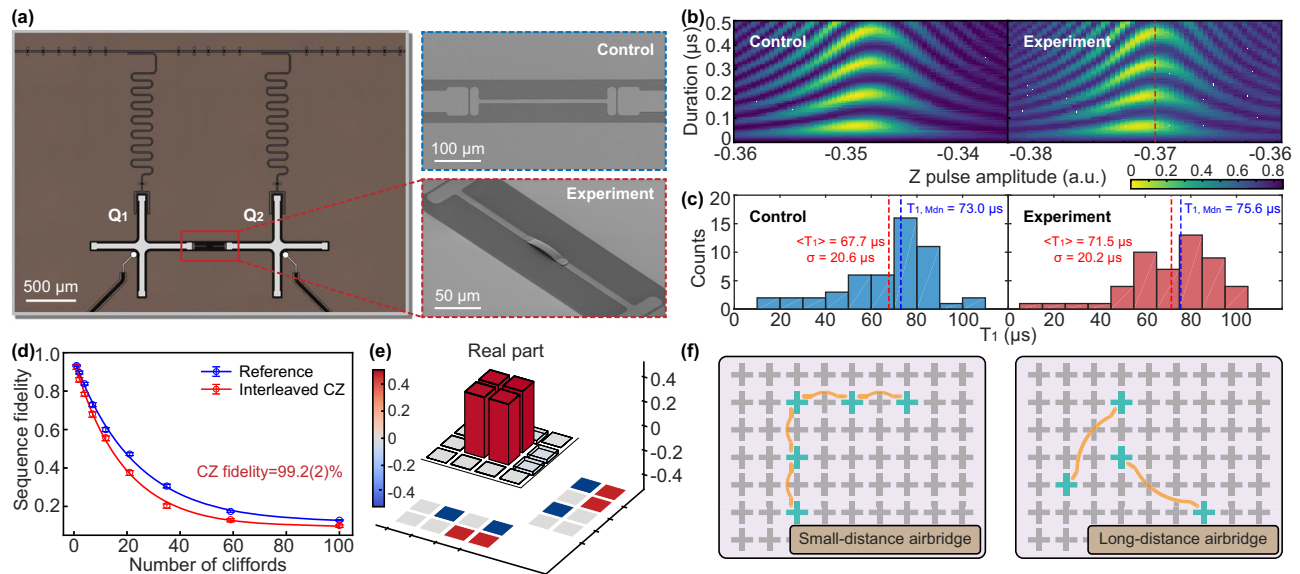


Fig. 5 | Utilization of well-designed tantalum airbridges in a direct coupling element. **a** Optical micrograph of the plane two-qubit superconducting quantum chip coupled via the separate tantalum airbridge, with fully-capped structure incorporated over each control line. Zoom-in images of the coupling for both control group and experimental group are shown in the right panel respectively. **b** Characterization of effective coupling strength. The qubits in both groups are initially prepared in the $|01\rangle$ state (or $|10\rangle$ state), followed by fine-tuning the qubit frequencies to achieve resonance. The red dotted line in the experimental group represents the maximum resonance position where we extract the coupling strength to be 3.9 MHz. **c** T_1 distribution for both control group and experimental group. Here the red and blue dotted line represent the extracted average T_1 ($\langle T_1 \rangle$) and median T_1 ($T_{1,Mdn}$), respectively. The standard deviation is also

calculated as σ . It can be found that the coupling capacitor via airbridge seems to have little effect on qubit decoherence through comparison between control group and experiment group. **d** Interleaved-RB of diabatic CZ gate for the experimental group. The gate fidelity is measured at 99.2(2)% for both the experimental and the control group. **e** Preparation of Bell state $|\psi\rangle = (|01\rangle + |10\rangle)/\sqrt{2}$ using CZ gate in **(d)** with state fidelity measured to be 99.70% via QST. **f** Schematic diagrams of the airbridge coupling mechanism in superconducting quantum processors. Here we consider two potential airbridge structures for coupling. Left panel: Small-distance airbridge ($L_{ab} \leq 200 \mu\text{m}$ where L_{ab} is defined in Eq. (1)) realizing neighboring or next-neighboring qubit-qubit connection. Right panel: Long-distance airbridge ($L_{ab} > 200 \mu\text{m}$) realizing long distance qubit-qubit connection.

equipped with fully-capped tantalum airbridges based on tantalum films, with median T_1 exceeding $100 \mu\text{s}$ for most qubits, and consistent single-qubit gate fidelity for isolated-RB and simultaneous-RB. Finally, we explore the application of tantalum airbridges in coupling mechanism, achieving measured two-qubit CZ gate fidelity of 99.2(2)% without sacrificing coherence time. Our results demonstrate the reliability of the lift-off method for fabricating tantalum airbridges and its potential broad applications in quantum computation and quantum error correction.

Methods

Airbridge simulation

We have mentioned that for etching and lift-off methods, the maximum length for a structurally stable airbridge is $\sim 60 \mu\text{m}$, while it increases to $200 \mu\text{m}$ for airbridges fabricated by grayscale lithography. Hence, we hypothesize that the stability of the airbridge is influenced by the corresponding profile of the photoresist scaffold. To investigate this behavior, we simulate the formation of the scaffold. We judge that the arch-shaped scaffold is formed by adding two profiles of the edge scaffold with opposite directions after reflow. Therefore, we extract the edge profile of the reflowed photoresist and simulate the profile of the scaffold by adding two edge profiles together. The overlap distance of two profiles represents the length of the airbridge, and the sum height of profiles is the simulated profile of the scaffold. By approaching two edge profiles with different distances, we can obtain profiles of scaffold with different airbridge lengths.

For the etching and lift-off methods, an arch-shaped scaffold is formed by combining two edge profiles with opposite directions after undergoing a high-temperature reflow process. By extracting and simulating these edge profiles together, we find that they are nearly the same across different

lengths of airbridges. The simulated profiles consistently align with experimental data (Fig. 6a, b), revealing the appearance of plateaus in scaffolds when exceeding $60 \mu\text{m}$ in length. These plateaus could potentially explain why longer airbridges become unstable. We also extract height information from our simulated scaffolds and qualitatively compare it with the experimental data with various lengths, as depicted in Fig. 6d. Meanwhile, for grayscale airbridges in Fig. 6c, where exposure gray values precisely define their profile, a parabolic shape remains consistent regardless of length.

These results suggest that the edge of the photoresist plays a crucial role in determining scaffold structure and ultimately affects the stability of airbridges depending on its characteristics such as having an elongated tail-like feature. During the reflow process, arch-shaped edges are formed. Consequently, by adjusting the reflow temperature, it is possible to systematically modify the profile of edge scaffold. Utilizing the simulation described above, one can roughly estimate the maximum achievable lengths for stable airbridges after reflow without compromising structural integrity.

Parallel single-qubit gate operations

Quantum circuits can be executed more efficiently by running quantum gates in parallel. However, this parallel quantum computation is vulnerable to correlated errors such as microwave crosstalk and stray coupling^{40,59}. To assess the effectiveness of tantalum airbridges and tunable couplers in mitigating these errors, we benchmark the single-qubit gate performance using both isolated and simultaneous RB⁴⁰, as depicted in Fig. 7b. The idle frequencies of all thirteen qubits are also presented in Fig. 7a for reference. Our result demonstrates a small increase (0.013%) in single-qubit gate error probabilities, indicating that our device exhibits low microwave crosstalk and stray coupling.

Fig. 6 | Experimental and simulated profiles of airbridge scaffolds for etching and lift-off methods. **a** Experimental profiles of airbridge scaffolds for etching and lift-off methods. **b** Simulated profiles of scaffold for etching and lift-off methods. **c** Experimental profiles of airbridge scaffold for grayscale lithography method. Notice that curves in (a), (b), and (c) have been shifted for clarity and the length of the airbridges are also marked beside each curves. **d** The height of the airbridges versus the length for both experimental and simulation data.

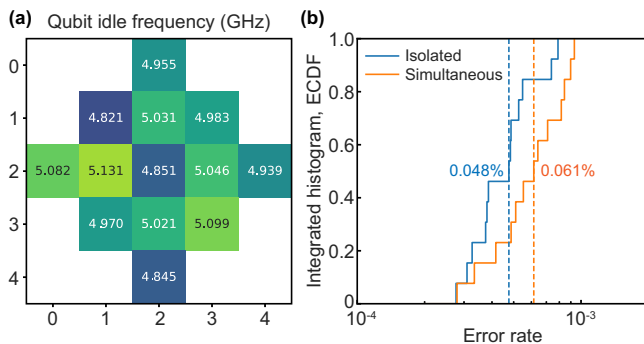
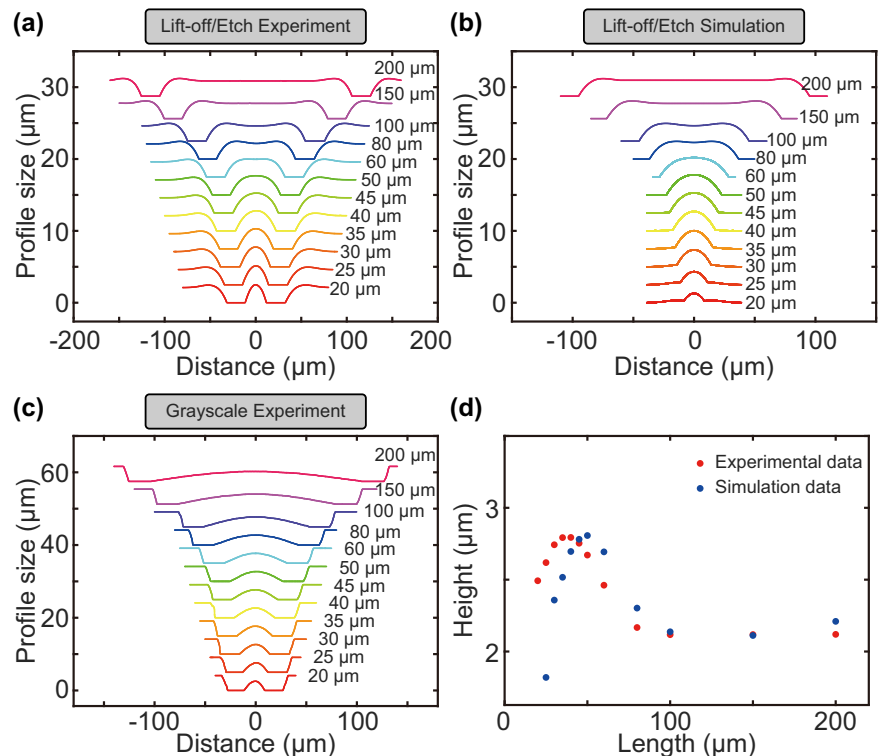


Fig. 7 | Characterization of parallel single-qubit gate operations. **a** Idle frequencies for all qubits when performing parallel single-qubit gate operation. **b** Integrated histogram (empirical cumulative distribution function, ECDF) of single-qubit Pauli errors, measured via isolated (blue) and simultaneous (orange) RB. The median of each distribution occurs at 0.5 marked by the dotted line with 0.048% for isolated-RB and 0.061% for simultaneous-RB (average values are similar).

Data availability

The data that support the findings of this study are available from the corresponding authors M.C.D., T.Q.C., and Y.C.Z. upon request.

Code availability

The codes that support the simulations of this study are available from the corresponding authors M.C.D., T.Q.C., and Y.C.Z. upon request.

Received: 12 January 2024; Accepted: 19 January 2025;

Published online: 29 January 2025

References

- Place, A. P. et al. New material platform for superconducting transmon qubits with coherence times exceeding 0.3 milliseconds. *Nat. Commun.* **12**, 1779 (2021).
- Müller, C., Lisenfeld, J., Shnirman, A. & Poletto, S. Interacting two-level defects as sources of fluctuating high-frequency noise in superconducting circuits. *Phys. Rev. B* **92**, 035442 (2015).
- De Graaf, S. et al. Two-level systems in superconducting quantum devices due to trapped quasiparticles. *Sci. Adv.* **6**, eabc5055 (2020).
- Thorbeck, T. et al. Two-level-system dynamics in a superconducting qubit due to background ionizing radiation. *PRX Quantum* **4**, 020356 (2023).
- Koch, J. et al. Charge-insensitive qubit design derived from the Cooper pair box. *Phys. Rev. A* **76**, 042319 (2007).
- Krantz, P. et al. A quantum engineer's guide to superconducting qubits. *Appl. Phys. Rev.* **6**, 021318 (2019).
- Chen, Z. et al. Fabrication and characterization of aluminum airbridges for superconducting microwave circuits. *Appl. Phys. Lett.* **104**, 052602 (2014).
- Murthy, A. A. et al. Developing a chemical and structural understanding of the surface oxide in a niobium superconducting qubit. *ACS Nano* **16**, 17257–17262 (2022).
- Altoé, M. V. P. et al. Localization and mitigation of loss in niobium superconducting circuits. *PRX Quantum* **3**, 020312 (2022).
- Verjauw, J. et al. Investigation of microwave loss induced by oxide regrowth in high-q niobium resonators. *Phys. Rev. Appl.* **16**, 014018 (2021).
- Kono, S. et al. Mechanically induced correlated errors on superconducting qubits with relaxation times exceeding 0.4 ms. *Nat. Commun.* **15**, 3950 (2024).
- Biznárová, J. et al. Mitigation of interfacial dielectric loss in aluminum-on-silicon superconducting qubits. *npj Quantum Inf.* **10**, 78 (2024).
- Wang, C. et al. Towards practical quantum computers: transmon qubit with a lifetime approaching 0.5 milliseconds. *npj Quantum Inf.* **8**, 3 (2022).
- Ganjam, S. et al. Surpassing millisecond coherence in on chip superconducting quantum memories by optimizing materials and circuit design. *Nat. Commun.* **15**, 3687 (2024).

15. Dunsworth, A. et al. A method for building low loss multi-layer wiring for superconducting microwave devices. *Appl. Phys. Lett.* **112**, 063502 (2018).
16. Abuwasib, M., Krantz, P. & Delsing, P. Fabrication of large dimension aluminum air-bridges for superconducting quantum circuits. *J. Vacuum Sci. Technol. B* **31**, 031601 (2013).
17. Jin, Y. et al. Microscopic metallic air-bridge arrays for connecting quantum devices. *Appl. Phys. Lett.* **118**, 162108(2021).
18. Girgis, E., Liu, J. & Benkheadar, M. Fabrication of metallic air bridges using multiple-dose electron beam lithography. *Appl. Phys. Lett.* **88**, 202103 (2006).
19. Janzen, N., Kononenko, M., Ren, S. & Lupascu, A. Aluminum air bridges for superconducting quantum devices realized using a single-step electron-beam lithography process. *Appl. Phys. Lett.* **121**, 094001 (2022).
20. Sun, Y. et al. Fabrication of airbridges with gradient exposure. *Appl. Phys. Lett.* **121**, 074001 (2022).
21. Stavenga, T. & DiCarlo, L. Lower-temperature fabrication of airbridges by grayscale lithography to increase yield of nanowire transmons in circuit QED quantum processors. *Appl. Phys. Lett.* **123**, 024004(2023).
22. Mukai, H. et al. Pseudo-2d superconducting quantum computing circuit for the surface code: proposal and preliminary tests. *N. J. Phys.* **22**, 043013 (2020).
23. O'Sullivan, J. et al. Deterministic generation of a 20-qubit two-dimensional photonic cluster state. *arXiv preprint arXiv:2409.06623* (2024).
24. Breuckmann, N. P. & Eberhardt, J. N. Quantum low-density parity-check codes. *PRX Quantum* **2**, 040101 (2021).
25. Fujiwara, Y., Clark, D., Vandendriessche, P., De Boeck, M. & Tonchev, V. D. Entanglement-assisted quantum low-density parity-check codes. *Phys. Rev. A* **82**, 042338 (2010).
26. Strikis, A. & Berent, L. Quantum low-density parity-check codes for modular architectures. *PRX Quantum* **4**, 020321 (2023).
27. Kovalev, A. A. & Pryadko, L. P. Fault tolerance of quantum low-density parity check codes with sublinear distance scaling. *Phys. Rev. A* **87**, 020304 (2013).
28. Panteleev, P. & Kalachev, G. Degenerate quantum ldpc codes with good finite length performance. *Quantum* **5**, 585 (2021).
29. Panteleev, P. & Kalachev, G. Quantum ldpc codes with almost linear minimum distance. *IEEE Trans. Inf. Theory* **68**, 213–229 (2021).
30. Yanay, Y. et al. Mediated interactions beyond the nearest neighbor in an array of superconducting qubits. *Phys. Rev. Appl.* **17**, 034060 (2022).
31. Liu, R., Liang, M.-L. & Yuan, B. Entanglement in the three-qubit heisenberg model with next nearest neighbor interaction and a nonuniform magnetic field. *Eur. Phys. J. D.* **41**, 571–578 (2007).
32. Song, C. et al. 10-qubit entanglement and parallel logic operations with a superconducting circuit. *Phys. Rev. Lett.* **119**, 180511 (2017).
33. Zhao, P. et al. Switchable next-nearest-neighbor coupling for controlled two-qubit operations. *Phys. Rev. Appl.* **14**, 064016 (2020).
34. Knill, E. et al. Randomized benchmarking of quantum gates. *Phys. Rev. A* **77**, 012307 (2008).
35. Jones, S. G. et al. Grain size in low loss superconducting Ta thin films on c axis sapphire. *J. Appl. Phys.* **134**, 144402 (2023).
36. Dorrani, D., Solati, E., Hantezadeh, M., Ghoranneviss, M. & Sari, A. Effects of low temperature on the characteristics of tantalum thin films. *Vacuum* **86**, 51–55 (2011).
37. Li, Y. et al. A parametric EDA method for coplanar waveguide channel recognition and air-bridge construction in quantum chip design. *IEEE Trans. Comput.-Aided Design of Integr. Circuits Syst.* **43**, 3004–3014(2024).
38. Megrant, A. et al. Planar superconducting resonators with internal quality factors above one million. *Appl. Phys. Lett.* **100**, 113510(2012).
39. Wang, H. et al. Improving the coherence time of superconducting coplanar resonators. *Appl. Phys. Lett.* **95**, 233508 (2009).
40. Arute, F. et al. Quantum supremacy using a programmable superconducting processor. *Nature* **574**, 505–510 (2019).
41. Wu, Y. et al. Strong quantum computational advantage using a superconducting quantum processor. *Phys. Rev. Lett.* **127**, 180501 (2021).
42. Shi, Y.-H. et al. Quantum simulation of topological zero modes on a 41-qubit superconducting processor. *Phys. Rev. Lett.* **131**, 080401 (2023).
43. Conner, C. et al. Superconducting qubits in a flip-chip architecture. *Appl. Phys. Lett.* **118**, 232602 (2021).
44. Rosenberg, D. et al. 3d integrated superconducting qubits. *npj Quantum Inf.* **3**, 42 (2017).
45. Yan, F. et al. Tunable coupling scheme for implementing high-fidelity two-qubit gates. *Phys. Rev. Appl.* **10**, 054062 (2018).
46. Li, X. et al. Tunable coupler for realizing a controlled-phase gate with dynamically decoupled regime in a superconducting circuit. *Phys. Rev. Appl.* **14**, 024070 (2020).
47. Ku, L.-C. & Clare, C. Y. Decoherence of a Josephson qubit due to coupling to two-level systems. *Phys. Rev. B* **72**, 024526 (2005).
48. Reed, M. *Entanglement and Quantum Error Correction with Superconducting Qubits. Ph.D thesis* (Yale University, 2013).
49. Barrett, C. N. et al. Learning-based calibration of flux crosstalk in transmon qubit arrays. *Phys. Rev. Appl.* **20**, 024070 (2023).
50. Dai, X. et al. Calibration of flux crosstalk in large-scale flux-tunable superconducting quantum circuits. *PRX Quantum* **2**, 040313 (2021).
51. Nuerbolati, W. et al. Canceling microwave crosstalk with fixed-frequency qubits. *Appl. Phys. Lett.* **120**, 174001 (2022).
52. Yan, H. et al. Calibration and cancellation of microwave crosstalk in superconducting circuits. *Chin. Phys. B* **32**, 094203 (2023).
53. Kosen, S. et al. Signal crosstalk in a flip-chip quantum processor. *PRX Quantum* **5**, 030350 (2024).
54. Wang, T. et al. Experimental realization of a fast controlled-z gate via a shortcut to adiabaticity. *Phys. Rev. Appl.* **11**, 034030 (2019).
55. Kannan, B. et al. Waveguide quantum electrodynamics with superconducting artificial giant atoms. *Nature* **583**, 775–779 (2020).
56. Kockum, A. F., Johansson, G. & Nori, F. Decoherence-free interaction between giant atoms in waveguide quantum electrodynamics. *Phys. Rev. Lett.* **120**, 140404 (2018).
57. Yin, X.-L. & Liao, J.-Q. Generation of two-giant-atom entanglement in waveguide-qed systems. *Phys. Rev. A* **108**, 023728 (2023).
58. Fowler, A. G., Mariantoni, M., Martinis, J. M. & Cleland, A. N. Surface codes: towards practical large-scale quantum computation. *Phys. Rev. A* **86**, 032324 (2012).
59. Google Quantum AI. Suppressing quantum errors by scaling a surface code logical qubit. *Nature* **614**, 676–681 (2023).
60. Xu, H. et al. Realization of adiabatic and diabatic cz gates in superconducting qubits coupled with a tunable coupler. *Chin. Phys. B* **30**, 044212 (2021).
61. Marxer, F. et al. Long-distance transmon coupler with cz-gate fidelity above 99.8%. *PRX Quantum* **4**, 010314 (2023).
62. Huai, S. et al. in preparation (2024).
63. Aleksey N, B. et al. Highly stable aluminum air-bridges with stiffeners. *arXiv preprint arXiv:2410.23028* (2024).

Acknowledgements

We thank Mengyu Zhang, Fuming Liu, Guanglei Xi, Qiaonian Yu, and Hualiang Zhang for supporting room-temperature electronics. We thank Shuoming An for providing Josephson parametric amplifiers. This work is supported by Shenzhen Science and Technology Program.

Author contributions

K.L.B. developed the lift-off method and fabricated the devices. T.Q.C., S.N.H., Y.C.Z. conceived the experiment. H.S.N., T.Q.C., Z.X.Z. established

the measurement setup and performed experimental measurements with the assistance of K.L.B., D.F.L., Y.L., J.J.H., X.P.Y., M.C.D., Y.C.Z., and S.Y.Z. K.L.B., T.Q.C., Y.C.Z. wrote the manuscript with feedback from all authors. T.Q.C., M.C.D., Y.C.Z. supervised the project. All authors contributed to the discussion of the results and the development of the manuscript.

Competing interests

The authors declare no competing interests.

Additional information

Supplementary information The online version contains supplementary material available at <https://doi.org/10.1038/s41534-025-00972-8>.

Correspondence and requests for materials should be addressed to Maochun Dai, Tianqi Cai or Yi-Cong Zheng.

Reprints and permissions information is available at <http://www.nature.com/reprints>

Publisher's note Springer Nature remains neutral with regard to jurisdictional claims in published maps and institutional affiliations.

Open Access This article is licensed under a Creative Commons Attribution-NonCommercial-NoDerivatives 4.0 International License, which permits any non-commercial use, sharing, distribution and reproduction in any medium or format, as long as you give appropriate credit to the original author(s) and the source, provide a link to the Creative Commons licence, and indicate if you modified the licensed material. You do not have permission under this licence to share adapted material derived from this article or parts of it. The images or other third party material in this article are included in the article's Creative Commons licence, unless indicated otherwise in a credit line to the material. If material is not included in the article's Creative Commons licence and your intended use is not permitted by statutory regulation or exceeds the permitted use, you will need to obtain permission directly from the copyright holder. To view a copy of this licence, visit <http://creativecommons.org/licenses/by-nc-nd/4.0/>.

© The Author(s) 2025